Enhanced Li+ Transport in Ionic Liquid-Based Electrolytes Aided by Fluorinated Ethers for Highly Efficient Lithium Metal Batteries with Improved Rate Capability

Xu Liu, Maider Zarrabeitia, Alessandro Mariani, Xinpei Gao, Hanno Maria Schütz, Shan Fang, Thomas Bizien, Giuseppe Antonio Elia, and Stefano Passerini**

FSI⁻-based ionic liquids (ILs) are promising electrolyte candidates for long-life and safe lithium metal batteries (LMBs). However, their practical application is hindered by sluggish Li+ transport at room temperature. Herein, it is shown that additions of bis(2,2,2-trifluoroethyl) ether (BTFE) to LiFSI-Pyr$_{14}$FSI ILs can effectively mitigate this shortcoming, while maintaining ILs' high compatibility with lithium metal. Raman spectroscopy and small-angle X-ray scattering indicate that the promoted Li+ transport in the optimized electrolyte, [LiFSI]$_3$[Pyr$_{14}$FSI]$_4$[BTFE]$_4$ (Li$_3$Py$_4$BT$_4$), originates from the reduced solution viscosity and increased formation of Li+-FSI⁻ complexes, which are associated with the low viscosity and non-coordinating character of BTFE. As a result, Li/LiFePO$_4$ (LFP) cells using Li$_3$Py$_4$BT$_4$ electrolyte reach 150 mAh g⁻¹ at 1 C rate (1 mA cm⁻²) and a capacity retention of 94.6% after 400 cycles, revealing better characteristics with respect to the cells employing the LiFSI-Pyr$_{14}$FSI (operate only a few cycles) and commercial carbonate (80% retention after only 218 cycles) electrolytes. A wide operating temperature (from −10 to 40 °C) of the Li/Li$_3$Py$_4$BT$_4$/LFP cells and a good compatibility of Li$_3$Py$_4$BT$_4$ with LiNi$_{0.5}$Mn$_{0.3}$Co$_{0.2}$O$_2$ (NMC532) are demonstrated also. The insight into the enhanced Li+ transport and solid electrolyte interphase characteristics suggests valuable information to develop IL-based electrolytes for LMBs.

1. Introduction

High-capacity lithium metal (3860 mAh g⁻¹) is considered a promising alternative to graphite (372 mAh g⁻¹) as anode material for the next-generation of high-energy-density batteries.[1] However, its high reactivity and unstable solid electrolyte interphase (SEI) formed in carbonate-based electrolytes lead to continuous chemical/electrochemical side reactions as well as unavoidable lithium dendrite formation, further causing consumptions of electrolytes, expansions of lithium metal, and generations of "dead lithium" upon cycling, which have obstacled the commercialization of room-temperature lithium metal batteries (LMBs).[2] In addition, uncontrollable heat generation from the side reactions, growing cell resistance, and internal short circuit, together with the flammable electrolyte, makes safety another severe issue.[3] Several strategies have been designed to improve the overall performance, including the lifespan and safety, such as 3D or/and lithiophilic host,[4] surface coating/artificial SEI,[5] and electrolyte engineering.[6] The latest one is particularly relevant, as it can intrinsically tune the lithium/electrolyte interface compatibility, lithium deposition morphology, and electrolyte flammability.[7]

Room-temperature ionic liquids (ILs, i.e., molten salts at room temperature) exhibit high thermal stability, nonvolatility, and low flammability.[8] Their physical and electrochemical properties are tightly associated with their structure. Bis(trifluoromethanesulfonyl)imide (TFSI⁻) and bis(fluorosulfonyl)imide (FSI⁻) are the most used anions of ILs-based electrolytes for high-voltage batteries. With more delocalized negative charge (−F exhibits stronger electron-withdrawing effect than −CF$_3$) and shorter chain,[9,10] FSI⁻ has weaker interactions with the neighboring cations than TFSI⁻, endowing FSI⁻-based ILs lower melting points and viscosities, and higher ionic conductivities.[11] Meanwhile, the SO$_2$−F bonds in FSI⁻ are weaker than the C−F bonds in TFSI⁻ and thus easier to be broken for the formation of F-rich SEI on lithium metal.[12,13] Therefore, the FSI⁻-based ILs show better compatibility with lithium metal anodes (LMAs) than the TFSI⁻-based ILs.[14] For instance, our group reported high Columbic efficiency (CE), that is, 99.1%, upon plating/stripping of lithium metal using [LiFSI]$_{0.1}$[Pyr$_{14}$FSI]$_{0.9}$ (Pyr$_{14}$FSI=N-butyl-N-methylpyrrolidinium bis(fluorosulfonyl)imide)

X. Liu, Dr. M. Zarrabeitia, Dr. A. Mariani, Dr. X. P. Gao, H. M. Schütz,
Dr. S. Fang, Dr. G. A. Elia, Prof. S. Passerini
Helmholtz Institute Ulm (HIU)
Helmholtzstraße 11, D-89081 Ulm, Germany
X. Liu, Dr. M. Zarrabeitia, Dr. A. Mariani, Dr. X. P. Gao, H. M. Schütz,
Dr. S. Fang, Dr. G. A. Elia, Prof. S. Passerini
Karlsruhe Institute of Technology (KIT)
P.O. Box 3640, D-76021 Karlsruhe, Germany
E-mail: giuseppe.elia@kit.edu; stefano.passerini@kit.edu
T. Bizien
SWING beamline
SOLEIL Synchrotron
L'Orme des Merisiers, Saint-Aubin 91190, France

as the electrolyte.[15] However, the application of these FSI−-based IL electrolytes is still hampered by their sluggish Li+ transport at room temperature (although the Li+ transport in the FSI−-based IL electrolytes is enhanced with respect to other ILs).[16,17] The limited Li+ transport in IL-based electrolytes is generally attributed to the high viscosity, but complex ion interactions and ion transport mechanisms, playing relevant roles, are still not clear. Hence, explorations on feasible strategies being able to mitigate the drawback mentioned above and further investigations on the mechanism behind are important and meaningful for developing FSI−-based IL electrolytes for LMBs application.

Fluorinated ethers are a new type of co-solvents recently introduced to mitigate the high viscosity and Li+ transport limitation of highly concentrated electrolytes employing, for example, ethers, carbonates, phosphonates, and sulfones based solvents.[18–26] With their non-solvating character, the fluorinated ethers poorly affect the solvation of Li+ ions, and therefore do not compromise the electrochemical properties of the matrix, for example, high plating/stripping efficiency.[20–23] Moreover, the fluorinated ethers exhibit low viscosity, reducing the overall viscosity of the electrolytes.[20–23] Therefore, adding fluorinated ethers to the FSI−-based IL electrolytes is expected to be an effective method to mitigate the sluggish Li+ transport in these electrolytes.

Herein, we propose the use of bis(2,2,2-trifluoroethyl) ether (BTFE) as co-solvent for LiFSI-Pyr$_{14}$FSI electrolytes. The influence of the molar ratio of Li+ against Pyr$_{14}^+$ and BTFE against Pyr$_{14}^+$ has been screened. The optimized electrolyte, [LiFSI]$_3$[Pyr$_{14}$FSI]$_4$[BTFE]$_4$, maintains high Li stripping/plating *CE* and exhibits thoroughly improved Li+ transports, resulting in excellent cycling stability and improved rate capability of the Li/Li and Li/LiFePO$_4$ (LFP) cells. Additionally to the basic physical and electrochemical properties, the ion interaction in the electrolytes, solution structure, and lithium deposition behavior as well as SEI chemical composition were also carefully investigated to elucidate the high compatibility with the LMA and the enhanced Li+ transport in the optimized [LiFSI]$_3$[Pyr$_{14}$FSI]$_4$[BTFE]$_4$ electrolyte. The operative temperature's influence on the rate performance of Li/LFP cells was also evaluated, as well as the compatibility of the electrolyte toward NMC532.

2. Results and Discussion

Figure S1, Supporting Information compares Li stripping/deposition behavior of LiFSI-Pyr$_{14}$FSI-BTFE electrolytes with a fixed BTFE:Pyr$_{14}$FSI molar ratio of 1:2, but different LiFSI:Pyr$_{14}$FSI molar ratios. Increasing LiFSI content results in improving the Li stripping/deposition process at high currents and prolonged cycle life. With the increased molar ratio of BTFE:Pyr$_{14}$FSI from 1:2 to 1:1, the best performance was obtained with the [LiFSI]$_3$[Pyr$_{14}$FSI]$_4$[BTFE]$_4$ formulation. Higher LiFSI: Pyr$_{14}$FSI, or BTFE:Pyr$_{14}$FSI molar ratios, for example, [LiFSI]$_4$[Pyr$_{14}$FSI]$_4$[BTFE]$_4$ and [LiFSI]$_3$[Pyr$_{14}$FSI]$_4$[BTFE]$_6$, result in a liquid–liquid phase separation as shown in Figure S2, Supporting Information. Thereafter, three IL-based electrolytes, that is, [LiFSI]$_1$[Pyr$_{14}$FSI]$_4$ (Li$_1$Py$_4$, low lithium content), [LiFSI]$_3$[Pyr$_{14}$FSI]$_4$ (Li$_1$Py$_4$, high lithium content), and [LiFSI]$_3$[Pyr$_{14}$FSI]$_4$[BTFE]$_4$ (Li$_3$Py$_4$BT$_4$ high lithium content with BTFE) were selected for further investigation in the following sections.

2.1. Physical and Electrochemical Properties

Figure 1a,b displays the viscosity and ionic conductivity of the IL-based electrolytes at different temperatures, respectively. Tables S1,S2, Supporting Information report the specific values. For LiFSI-Pyr$_{14}$FSI binary electrolytes, higher viscosities and lower ionic conductivities are observed upon increasing LiFSI fraction. The addition of BTFE to Li$_3$Py$_4$, however, brings back the viscosity and ionic conductivity values to the level of Li$_1$Py$_4$. Slightly lower viscosity and ionic conductivity characterize the Li$_3$Py$_4$BT$_4$ formulation with respect to the Li$_1$Py$_4$. In addition, the apparent transference number of Li+ was measured via the direct current polarization method.[27] The electrochemical impedance spectra taken before and after the polarization and the current evolution upon time are shown in Figure S3, Supporting Information. For LiFSI-Pyr$_{14}$FSI binary electrolytes, a higher Li+ fraction results in the increase of the Li+ transference number from 0.099 for Li$_1$Py$_4$ to 0.160 for Li$_3$Py$_4$. Both the value and trend are similar to the previously reported ones.[28] Interestingly, Li$_3$Py$_4$BT$_4$ exhibits a slightly higher Li+ transference number, that is, 0.184, than Li$_3$Py$_4$. Considering the measured Li+ transference numbers and the ionic conductivities, one can find that the Li+ transport is highly enhanced in Li$_3$Py$_4$BT$_4$ compared to Li$_1$Py$_4$ and Li$_3$Py$_4$.[29]

Figure 1c shows the Walden plots obtained from the measured viscosities, ionic conductivities, and densities (Table S3, Supporting Information) of the IL-based electrolytes at various temperatures, according to Equation (1).[30,31]

$$\log \Lambda = \log C + \alpha \log \frac{1}{\eta} \tag{1}$$

Here, Λ (S cm^2 mol^{-1}) is the molar conductivity, η (Poise) is the viscosity, and α is an adjustable parameter. All the investigated compositions fall below the KCl line reference, representing the "ideal" solution where the ions are fully dissociated and ion–ion interactions can be neglected. Thus, ion–ion interactions occur in the IL-based electrolytes.

In Equation (1), $\log C$ represents the distance from the "ideal" aqueous KCl line ($\alpha = 1$, $\log C = 0$) and the strength of the ion association.[32] $\log C$ values for Li$_1$Py$_4$ and Li$_3$Py$_4$ are −0.192 and −0.319, respectively, indicating that the addition of more LiFSI (higher Li+ concentration) leads to stronger ion association in the LiFSI-Pyr$_{14}$FSI binary system. Surprisingly, the dilution of the Li$_3$Py$_4$ with BTFE leads to a slightly lower $\log C$, that is, −0.327, indicating a stronger ion association despite a lower Li+ concentration.

The electrolytes' electrochemical anodic stability was evaluated via the linear sweep voltammograms measured using C65 coated Al foil as working electrode with a scan rate of 0.1 mV s^{-1}. As shown in Figure 1d, a negligible current density (<2 μA cm^{-2}) is recorded for potential below 4.4 V versus Li/Li+ for all the investigated formulations, suggesting possible compatibility of the investigated electrolytes with conventional cathode materials, for example, LFP and NMC cathodes.

2.2. Ion Interactions and Solution Structures

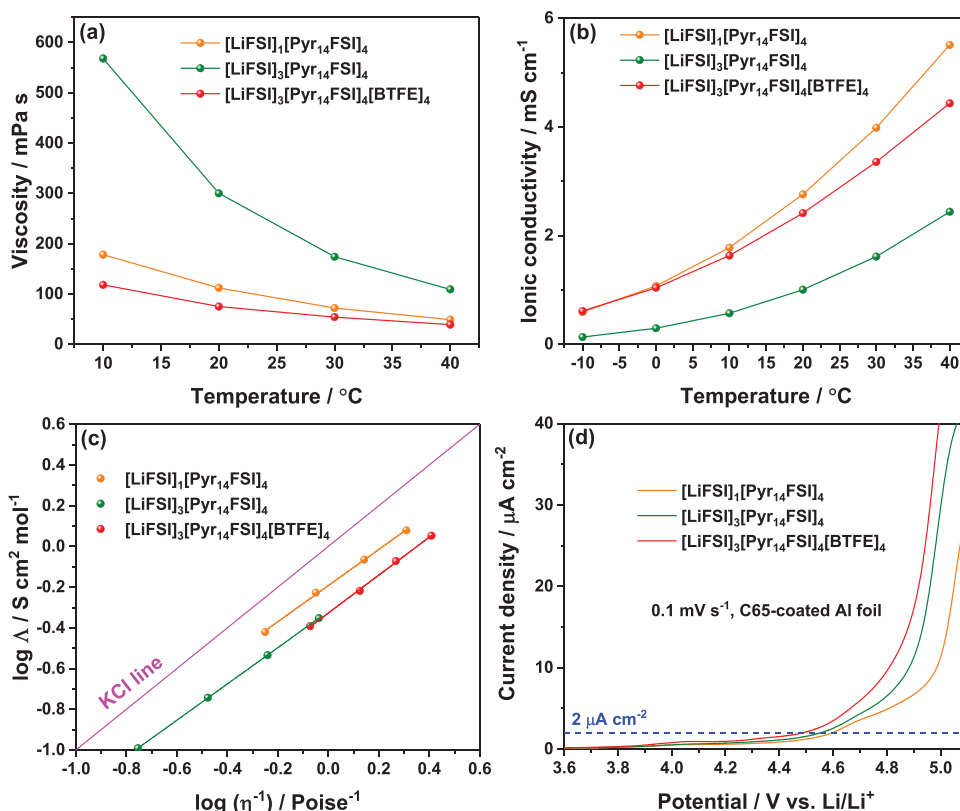The ion interactions in the electrolytes were further characterized via Raman spectroscopy. The peaks at 1200–1250 cm^{-1}

**ADVANCED
SCIENCE NEWS**

www.advancedsciencenews.com

**small
methods**

www.small-methods.com

Figure 1. a) Viscosities, b) ionic conductivities, and c) Walden plots of the IL-based electrolytes at different temperatures. d) The linear sweep voltammograms of the C65-coated Al working electrodes in the IL-based electrolytes with a scan rate of 0.1 mV s⁻¹.

originate from the −SO_2- group of the FSI^-, as displayed in **Figure 2**a.[33] In neat $Pyr_{14}FSI$, the peak (peak 1) located at 1216 cm⁻¹ is assigned to "free" FSI^-, which only weakly interacts with Pyr_{14}^+ due to the low charge density and large size of the cation. The addition of LiFSI to the system leads to the formation of a new shoulder peak (peak 2) located at a higher Raman shift, that is, 1225 cm⁻¹ for Li_1Py_4 and 1228 cm⁻¹ for Li_3Py_4. Peak 2 is associated with the coordination of FSI^- with Li^+ due to the higher charge density of Li^+.[34] The higher Raman shift of peak 2 in Li_3Py_4 with respect to Li_1Py_4 suggests higher levels of ion-pairing, such as doubles, triples, and polymer-like aggregates.[35] The comparison of Li_3Py_4 and $Li_3Py_4BT_4$ spectra does not evidence dramatic change, demonstrating that the coordination between Li^+ and FSI^- is not substantially affected by BTFE addition. The fraction of Li^+-coordinated FSI^- (f) can be calculated according to Equation (2):[36]

$$f = \frac{A_2}{A_1 + A_2} \tag{2}$$

where A_1 and A_2 are the areas of the peak 1 and 2, respectively. The calculated f for Li_1Py_4, Li_3Py_4, and $Li_3Py_4BT_4$ is 0.564, 0.891, and 0.926, respectively. The results indicate that nearly half of FSI^- are in the "free" state in Li_1Py_4, while most FSI^- coordinate with Li^+ in both Li_3Py_4 and $Li_3Py_4BT_4$. Since Li^+ has a higher charge density than Pyr_{14}^+, the increase of f is expected when more LiFSI is dissolved in $Pyr_{14}FSI$, which is also the reason for the observed higher viscosities of Li_3Py_4.

The slightly higher f in $Li_3Py_4BT_4$ than in Li_3Py_4 indicates that BTFE promotes FSI^- to solvate Li^+, despite the lower overall Li^+ concentration in $Li_3Py_4BT_4$. The obtained f agrees with the ion association strength predicted from the Walden plots (Figure 1c). Thereafter, the average number of FSI^- coordinating to each Li^+ (n) can be further calculated according to Equation (3):[36]

$$n = \frac{f}{x} \tag{3}$$

where x is the molar fraction of Li^+ with respect to all cations (i.e., Li^+ and Pyr_{14}^+). The resulting values of n for Li_1Py_4, Li_3Py_4, and $Li_3Py_4BT_4$ are 2.82, 2.08, and 2.16, respectively.

Figure 2b shows that the peaks located at 292 and 359 cm⁻¹ are associated with the FSI^- anti-conformer, while the 298 and 355 cm⁻¹ peak are associated with the FSI^- syn-conformer.[37,38] The ball-stick models of these two conformers are shown in Figure S4, Supporting Information. These two conformers coexist in equilibrium in the electrolytes. In neat $Pyr_{14}FSI$, the anti-conformer dominates. When LiFSI is dissolved in $Pyr_{14}FSI$, the equilibrium shifts toward the syn-conformer. In Li_3Py_4, the syn-conformer becomes the majority. Such a syn-conformer-dominated feature is maintained in the $Li_3Py_4BT_4$. It has been proposed that the binding energy of Li^+ with the syn-conformer is lower than with the anti-conformer.[35] Since these peaks overlap the signal from Pyr_{14}^+,[37] they cannot be fitted for a quantitative conformer evaluation. But the influence of the

**ADVANCED
SCIENCE NEWS**

www.advancedsciencenews.com
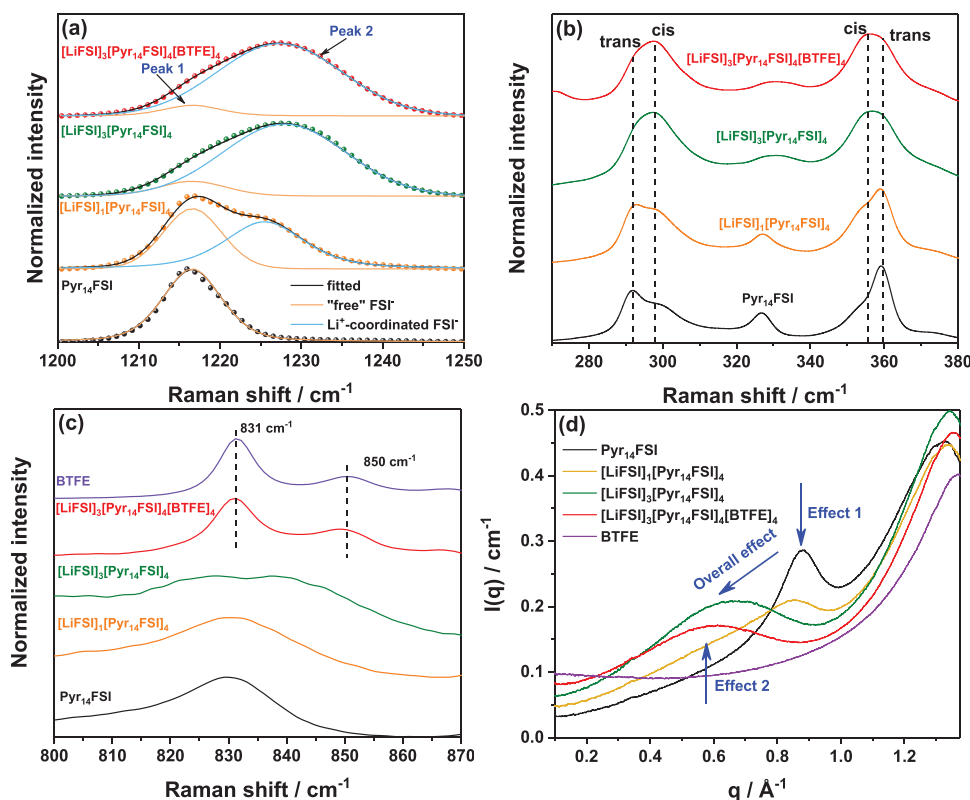
**small
methods**

www.small-methods.com

Figure 2. a–c) Raman spectra of the IL-based electrolytes at room temperature in different Raman shift regions. For comparison, those of BTFE or/and Pyr$_{14}$FSI are also displayed. d) The SAXS spectra of BTFE, Pyr$_{14}$FSI, and the IL-based electrolytes at room temperature.

LiFSI fraction and BTFE fraction on the conformer equilibrium is clear.

The Raman spectra at 800–870 cm^{-1} are shown in Figure 2c. Pyr$_{14}$FSI and LiFSI-Pyr$_{14}$FSI spectra reveal a broad peak around 830 cm^{-1}, which can be attributed to ν_{as}SNS mode of FSI$^-$.[33] Its shift toward higher Raman shift upon increasing LiFSI fraction reflects the formation of higher levels of Li$^+$-FSI$^-$ ion-pairing, which is similar to what is observed in Figure 2a.[35] When the Li$_3$Py$_4$ is diluted with BTFE, two sharper peaks located at 831 and 850 cm^{-1} arise. The position of these peaks matches well with the spectra of BTFE, indicating that these peaks originate from BTFE, but that BTFE is not involved in strong ion-solvent interactions, for example, Li$^+$-BTFE.[20,39] This phenomenon agrees well with the insolubility of LiFSI in pure BTFE.[22] The non-solvating character of BTFE toward Li$^+$ can explain the minimal change in ion association strength, that is, the fraction of Li$^+$-coordinated to FSI$^-$, the average number of FSI$^-$ coordinating to each Li$^+$, and the predominance of the FSI$^-$ syn-conformer in Li$_3$Py$_4$BT$_4$ despite of an overall lower Li$^+$ concentration than in Li$_3$Py$_4$. The capability of BTFE as co-solvent to maintain these features, due to its non-solvating ability, is essential for the high performance of FSI$^-$-based IL electrolytes. In fact, when the non-solvating BTFE is replaced with dimethyl carbonate (DMC), also characterized by a low viscosity but with solvation capability toward Li$^+$, that is, [LiFSI]$_4$[Pyr$_{14}$FSI]$_4$[DMC]$_4$, the features observed in the Raman spectra and the high rate capability of Li/Li cells vanish, as shown in Figure S5, Supporting Information.

Small-angle X-ray scattering (SAXS) was performed to understand better the electrolytes' solution structure (Figure 2d). Two main features, that is, the main peak around 1.3–1.4 Å^{-1} and prepeak around 0.4–1.0 Å^{-1}, are observed in the examined q-range for all the samples except pure BTFE, which, as expected, shows only the main peak centered at ≈1.368 Å^{-1}. By applying the Bragg relationship $r = 2\pi/q$, it is possible to extract the characteristic distance responsible for the SAXS peaks. The results are summarized in **Table 1**. The main peak is associated with the first neighbor's interaction and gives structural information on the adjacent species' average distance. Li$^+$ strongly coordinated with FSI$^-$ explains the peak shift (shorter distance) in LiFSI-Pyr$_{14}$FSI with respect to the Pyr$_{14}$FSI where Pyr$_{14}^+$ has a larger size and steric hindrance. LiFSI addition to the system leads to the main peak shift toward the left because the relative weight of the Li$^+$-FSI$^-$ interaction increases, as also confirmed by the Raman results, where the "free" FSI$^-$ signal decreases upon LiFSI addition. More caution is required for the interpretation of the shifts in the BTFE-containing systems since two effects may be acting at the same time, namely, a solvent-induced shortening of the Li$^+$-FSI$^-$ correlation, and the BTFE main peak itself at higher q values than the other compounds here investigated.

More interesting is the behavior of the pre-peak. This feature is usually not observed for isotropic liquids, that is, BTFE, with the exception of some strongly amphiphilic molecular liquids[40,41] and some ILs.[42,43] This peak is due to supramolecular interactions with specific characteristic

Table 1. Peak positions and corresponding characteristic real length for the samples investigated with SAXS.

Samples	Main peak position [Å^{-1}]	Real length [Å]	Prepeak position [Å^{-1}]	Real length [Å]
$Pyr_{14}FSI$	1.327	4.735	0.882	7.124
$[LiFSI]_1[Pyr_{14}FSI]_4$	1.338	4.696	0.854	7.357
$[LiFSI]_3[Pyr_{14}FSI]_4$	1.343	4.678	0.666	9.434
$[LiFSI]_3[Pyr_{14}FSI]_4[BTFE]_4$	1.355	4.637	0.599	10.489
BTFE	1.368	4.593	–	–

lengths in the order of a few nanometers. For ILs, the feature's origin lies in the so-called "sponge-like" structure, consisting of a bicontinuous network of apolar and polar domains. The peak position is mostly determined by the alkyl chain's length on (usually) the cation. In the case of $Pyr_{14}FSI$, we find the maximum intensity at 0.882 Å^{-1}, corresponding to 7.124 Å and well matching the length of a butyl tail ($\approx$8 Å). LiFSI addition to the IL leads to a decrease in intensity coupled with a shift toward smaller q values of the peak. We cannot exclude that the shift originates from another feature emerging at smaller q values, as hinted by the asymmetry of the orange curve in Figure 2d. The formation of a new structure, with a larger dimension around 10 Å, becomes more evident by increasing the salt concentration (olive curve) and adding BTFE (red curve). Although this structure's specifics are still unknown and require further more in-depth investigation with the support of computational methods, it is reasonable to infer that the domain is associated, at least, with Li$^+$ and FSI$^-$ because this structure is highly dependent on the addition of Li$^+$ and BTFE. As discussed above, in the presence of BTFE, Li$^+$ is more strongly coordinated with FSI$^-$ since BTFE does not solvate Li$^+$, but favors for a stronger solvation of Li$^+$ by FSI$^-$.[44] The previously described Li$^+$-FSI$^-$ complex could be (part of) this new, larger structure observed in the SAXS.

Based on the Raman and SAXS results, the measured enhanced physical properties of $Li_3Py_4BT_4$ than Li_1Py_4 and Li_3Py_4 can be reasonably interpreted. For the LiFSI-$Pyr_{14}FSI$ binary solution with a low LiFSI fraction (e.g., Li_1Py_4), the ion association is weak, and Li$^+$, strongly coordinated by FSI$^-$, transports via a diffusion-controlled vehicular mechanism.[45] At elevated LiFSI content (Li_3Py_4), the ion association increases and most of FSI$^-$ coordinate with Li$^+$ forming the Li$^+$-FSI$^-$ complex, leading to higher viscosities, reduced ions' mobility, and lower ionic conductivity. However, in these conditions, the Li$^+$-FSI$^-$ average coordination number decreases and syn-conformer formation weakens Li$^+$-FSI$^-$ binding energy, unlocking a hopping-type transport through FSI$^-$ exchange in Li$^+$-FSI$^-$ complex.[35,36] Li$^+$-FSI$^-$ complex formed in $Li_3Py_4BT_4$ is even strengthened with respect to Li_3Py_4, further promoting the hopping-type transport of Li$^+$ in the Li$^+$-FSI$^-$ complex. At the same time, BTFE effectively decreases the mixture's viscosity and further enhances the mobility of the Li$^+$-FSI$^-$ complex and free ions, leading to an enhanced ionic conductivity. Therefore, retaining the Li$^+$-FSI$^-$ complex and decreasing the solution's viscosity are equally beneficial to the enhanced Li$^+$ transport in the FSI$^-$-based ILs, which could be valid in general for other IL-based compositions.

2.3. Rate Capability and Stability Against LMAs

The performance of the LMAs in the electrolytes was evaluated in Li/Li symmetric cells and Li/Cu cells. **Figure 3**a shows the Li/Li cells' voltage profiles in the initial cycles of plating/stripping using Li_1Py_4 and Li_3Py_4 at a current density of 0.5 mA cm^{-2} and an areal capacity of 1 mAh cm^{-2} for each stripping/plating step. In the initial discharge, the voltage suddenly increases from −0.07 to −0.02 V at around 0.4 mAh cm^{-2}, after which low polarization and rectangular profile is observed upon the following cycles, implying the occurrence of short circuits. The same behavior is confirmed in Li/Cu cells employing Li_1Py_4 and Li_3Py_4 at the same current density and deposited areal capacity. The sudden increase of the voltage is observed again in the initial discharge, and the voltage does not increase to the upper cut-off (1 V) upon the following charge. Moreover, the charge capacity is much higher than the discharge capacity, thus confirming a short circuit in the initial discharge. In contrast with other literature reports regarding IL-based electrolytes, the poor performance here mainly results from the higher current and areal capacity used in the tests.[46] When $Li_3Py_4BT_4$ is employed, the Li/Li cell operates well even at a high current density of 2.5 mA cm^{-2} with an overpotential comparable to the one using LP30, demonstrating a good rate capability (Figure 3c).

The Li stripping/plating CE of Li/Cu coin cells employing $Li_3Py_4BT_4$ and LP30 were evaluated using a current of 0.5 mA cm^{-2} and a deposited capacity of 0.5 mAh cm^{-2}. The results are summarized in Figure 3d. The initial CE is 97.9%. After the initial tens cycles, during which SEI formation occurs covering the Cu substrate, the CE increases to around 99% as shown in Figure 3d inset. This suggests high reversibility of the Li stripping/plating process in $Li_3Py_4BT_4$. Despite a similar initial CE, the cell employing LP30 shows fast CE decay and cannot operate after 65 cycles. The voltage profiles at the selected cycles are shown in Figure S6, Supporting Information. The cycling ability of the LMA in $Li_3Py_4BT_4$ was further assessed in Li/Li cells subjected to continuous galvanostatic cycling with a current density of 1 mA cm^{-2} and a cycling capacity of 1 mAh cm^{-2} (2 h per cycle). The voltage profiles are shown in Figure 3e. The LMA in LP30 electrolyte shows poor cycling stability (150 cycles), as already seen for the Li/Cu cell shown in Figure 3d. On the contrary, the cell employing $Li_3Py_4BT_4$ exhibits a remarkable lifespan and cycling ability (more than 450 cycles, 900 h) with a limited polarization, that is, 150 mV. The voltage profiles of the cells at selected cycles are shown in Figure S7, Supporting Information.

Figure 3f,g display the Nyquist plots of the Li/Li cells employing LP30 and $Li_3Py_4BT_4$ electrolytes, respectively, after
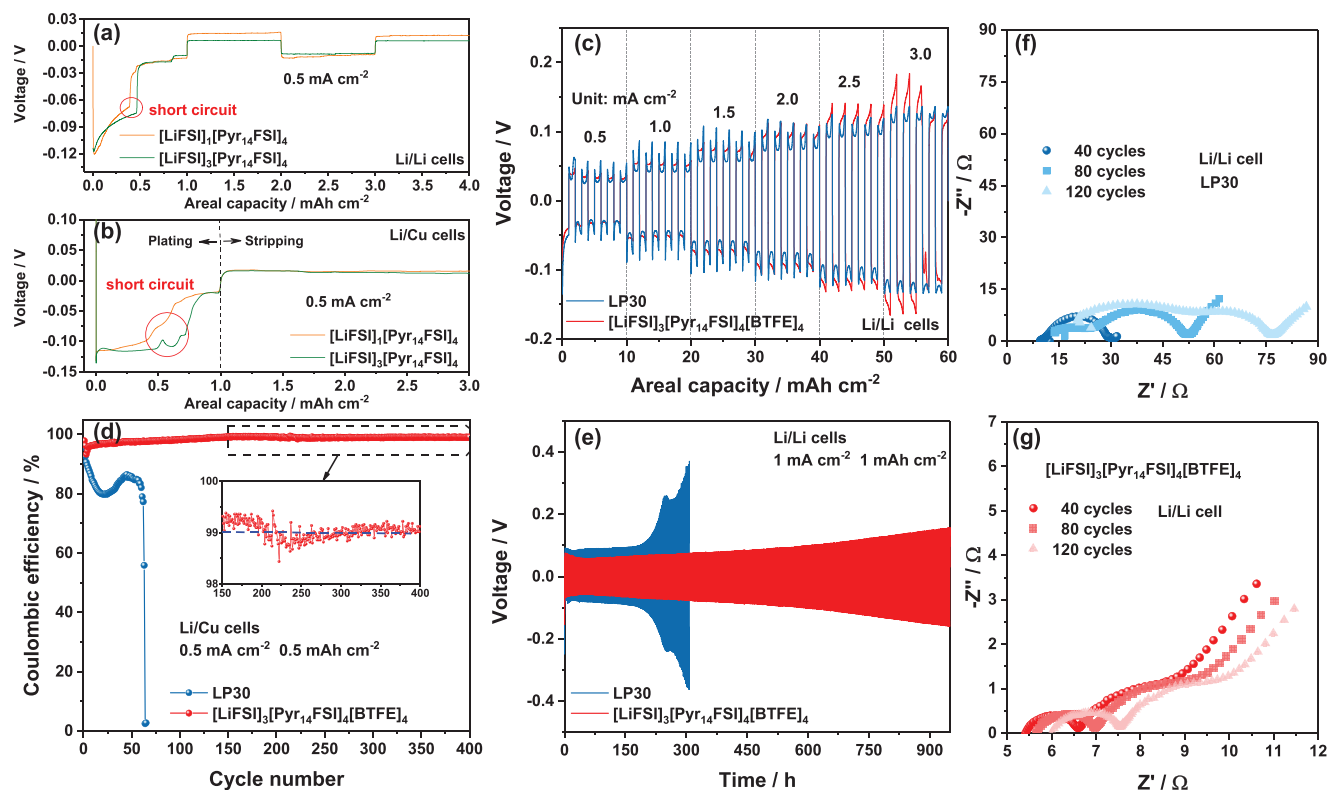
Figure 3. Voltage profiles of Li plating/stripping processes in a) Li/Li and b) Li/Cu coin cells employing Li_3Py_4 and Li_1Py_4 electrolytes. c) Voltage profiles of Li plating/stripping processes in Li/Li cells employing $Li_3Py_4BT_4$ and LP30 electrolytes at various current densities. d) *CE*s of Li plating/stripping upon cycling in $Li_3Py_4BT_4$ and LP30 electrolytes measured in Li/Cu cells. e) Long-term cycling voltage profiles for Li/Li cells using the $Li_3Py_4BT_4$ and LP30 electrolytes. Nyquist plots of the Li/Li cells using the f) LP30 and g) $Li_3Py_4BT_4$ electrolytes after certain cycles.

different Li stripping/plating cycles (1 mA cm⁻², 1 mAh cm⁻²). The Nyquist plots at the OCV state are shown in Figure S8, Supporting Information. The high-frequency intercept corresponds to a pure resistor associated with the bulk resistance of the electrolyte and lithium electrodes (ohmic resistance, R_s). Due to the inferior ionic conductivity of $Li_3Py_4BT_4$ to LP30 electrolyte, a slightly higher R_s is observed in the cell using $Li_3Py_4BT_4$ electrolyte. The depressed semicircle observed at lower frequencies is associated to the interfacial resistance (R_i).[47] Note that the native surface layer on LMA also contributes to the R_i. After 40 cycles in the $Li_3Py_4BT_4$ electrolyte, the plot is distinct from the OCV one. The decrease of the interfacial resistance can be attributed to the formation of a porous corrosion layer upon cycling and consequently increased surface area of the LMA. The three overlapping semicircles contributing to the interfacial resistance at high-frequency are associated with three interfacial structures in the corrosion layer on LMAs.[48] Similar features are also observed in the plots of the cell employing the LP30 electrolyte (Figure 3f). The evolution of ohmic and interfacial resistances upon cycling is quite different in the two electrolytes. In LP30, both R_s and R_i rapidly increase upon cycling, indicating the electrolyte's elevated decomposition and growth of the corroded lithium layer. In contrast, the cell impedance increase in the $Li_3Py_4BT_4$ is limited to few ohms from the 40th to the 120th cycle, indicating high chemical and electrochemical stabilities of $Li_3Py_4BT_4$ against LMAs. The EIS plot differences agree with the Li/Li

cells' polarization evolution upon stripping/deposition using the different electrolytes (Figure 3e).

Overall, the $Li_3Py_4BT_4$ outperforms LP30 in terms of reversibility and cyclability of LMAs, owing to improved interfacial compatibility, usually associated with the formed SEI and Li-metal deposition morphology.

2.4. Morphology of the Li-Metal Deposition and Cycled LMAs

The morphology of the Li (1.5 mAh cm⁻²) deposited at 0.5 mA cm⁻² in LP30 (**Figure 4**a,b) and $Li_3Py_4BT_4$ (Figure 4c,d) electrolytes on Cu foil was observed via scanning electron microscopy (SEM). From the SEM images of the surface, a clear morphology difference between the typical dendritic lithium observed in the LP30 electrolyte (Figure 4a) and the nodule-like Li particles with a size of tens of micrometers formed in $Li_3Py_4BT_4$ (Figure 4c) is evident. Larger Li particles effectively reduce the surface area and, consequently, the side reactions at the Li/electrolyte interface, thus being beneficial for both the reversibility of Li stripping/plating and the cyclability of LMAs. The Li particles' morphologic features observed from the surface are also visualized from the cross section (Figure 4b,d).

The evolution of Li metal with an initial thickness of 500 μm in symmetrical Li/Li cells cycled for 100 striping/plating cycles with a current density of 1 mA cm⁻² and a capacity of 1 mAh cm⁻² in $Li_3Py_4BT_4$ and LP30 was also investigated

ADVANCED
SCIENCE NEWS
www.advancedsciencenews.com
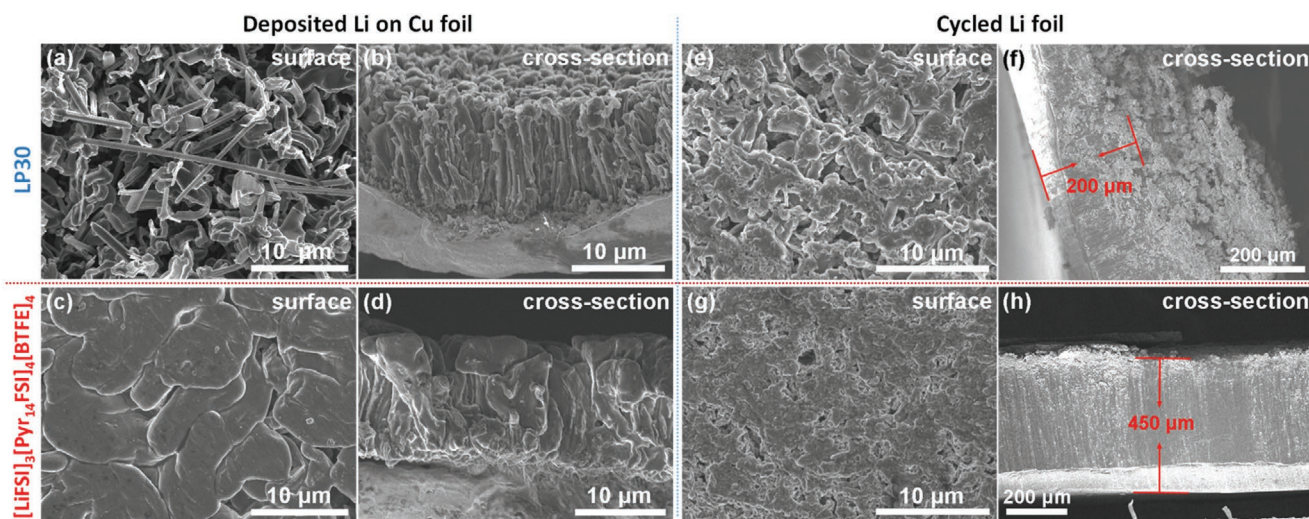
small
methods
www.small-methods.com

Figure 4. a,c) Surface and b,d) cross section morphology of the Li (1.5 mAh cm^{-2}) deposited at 0.5 mA cm^{-2} on Cu foils in the LP30 (a,b) and Li$_3$Py$_4$BT$_4$ (c,d) electrolytes. e,g) Surface and f,h) cross section morphology of the Li foil after 100 cycles with a current density of 1 mA cm^{-2} and a stripping-plating areal capacity of 1 mAh cm^{-2} in the LP30 (e,f) and Li$_3$Py$_4$BT$_4$ (g,h)electrolytes. The initial thickness of the Li foil is 500 μm.

by SEM. A porous surface is observed when LP30 is used (Figure 4e). Due to the severe lithium corrosion upon cycling in the LP30 electrolyte, large pieces of corroded lithium layer detouched from the electrode during the sample preparation for the cross section observation. Therefore, the accumulation of the porous layer cannot be seen. Nonetheless, the residual, uncorroded bulk lithium shows a rather limited thickness, for example, 200 μm (Figure 4f), evidencing an aggressive reaction of LP30 with LMA. Instead, when Li$_3$Py$_4$BT$_4$ is used, a denser surface is observed (Figure 4g), indicating rather limited lithium corrosion. Indeed, the corrosion layer in this electrolyte is rather limited, as the thickness of the uncorroded bulk lithium is measured to be 450 μm (Figure 4h).

2.5. The Surface Chemistry of LMAs

X-ray photoelectron spectroscopy (XPS) analysis of the Li metal deposited on Cu foil at a current density of 0.5 mA cm^{-2} (areal capacity: 1.5 mAh cm^{-2}) was performed to investigate the difference of the LMAs' surface chemistry in LP30 and Li$_3$Py$_4$BT$_4$. The results are displayed in **Figure 5**. Conventional SEI species from LP30 decomposition are detected, such as Li$_2$CO$_3$, O−C=O, C=O/C−O, and C−C/C−H from the solvents and Li$_x$PF$_y$ and Li$_x$PO$_y$F$_z$ from the salt (Figure 5a).[49–51] The relatively low concentration of CO$_3^{2-}$ peak in the C 1s and O 1s spectra and Li−O in the O 1s spectrum suggest that the SEI formed with LP30 is dominated by organic species. It has been reported that such an organic compound dominated SEI is preserved even at inner depth in these conventional carbonate electrolytes.[52]

Despite the different chemistries of LP30 and Li$_3$Py$_4$BT$_4$, several components and their relative contents in the SEI surface are similar, as evidenced by the C 1s, O 1s, and Li 1s spectra (Figure 5b). Since neither Pyr$_{14}^+$ nor FSI$^-$ contains C=O/C−O, its presence indicates BTFE decomposition during the SEI formation on LMAs. On the other hand, the

peak located around 286.4 eV in C 1s spectra, assigned to CN, originates from the decomposition of Pyr$_{14}^+$. In the O 1s spectra, the C−O peak clearly shifts to lower binding energy, resulting from the overlapping of the S−O (SO$_x$) feature from neat FSI$^-$ and its decomposition products. In the F 1s spectra, a low concentration of LiF is observed at 695 eV, while most of the F-based species result from BTFE decomposition (C−F at ≈690 eV) and FSI$^-$ (S−F at 686.6 eV) decomposition. These results indicate that all the electrolyte components, such as, Pyr$_{14}^+$, FSI$^-$, and BTFE, contribute to the SEI formation on LMAs.

The depth evolution of the chemical composition of the SEI formed in Li$_3$Py$_4$BT$_4$ was also examined (Figure 5b). The overall species composition does not vary as a function of the SEI thickness. With increasing sputtering time, the Li metal signal at ≈55.5 eV in Li 1s spectra increases,[53] while the signal intensity in C 1s and O 1s decreases. However, the C=O/C−O peak and C−O/S−O peak still dominate the C 1s and O 1s spectra, respectively. In the F 1s spectra, the F−C peak intensity does not show significant variation at different depths. Since these three peaks are only or mostly associated with the BTFE decomposition, it is reasonable to infer that BTFE builds the matrix of the SEI on the LMAs. Additionally, the intensity of the CN peak in the C 1s spectra, representing the decomposition of the Pyr$_{14}^+$, decreases upon higher depths, suggesting that the Pyr$_{14}^+$ decomposition mainly contributes to the outer layer of the SEI. The F−S and LiF's peak intensity in the F 1s spectra increases at the inner depths, proving more decomposition of the FSI$^-$. LiF is a good electric insulator with high mechanical strength that effectively blocks electron leakage through the SEI and limits Li growth at the electrolyte interface, leading to the high-performance of LMAs in Li$_3$Py$_4$BT$_4$.[54,55] The XPS analysis evidences that the SEI on LMA could be effectively tuned by selecting cation, anion, and fluorinated ethers, which endows the possibility of further optimizing the stability of the IL-fluorinated-ethers electrolyte against LMAs.
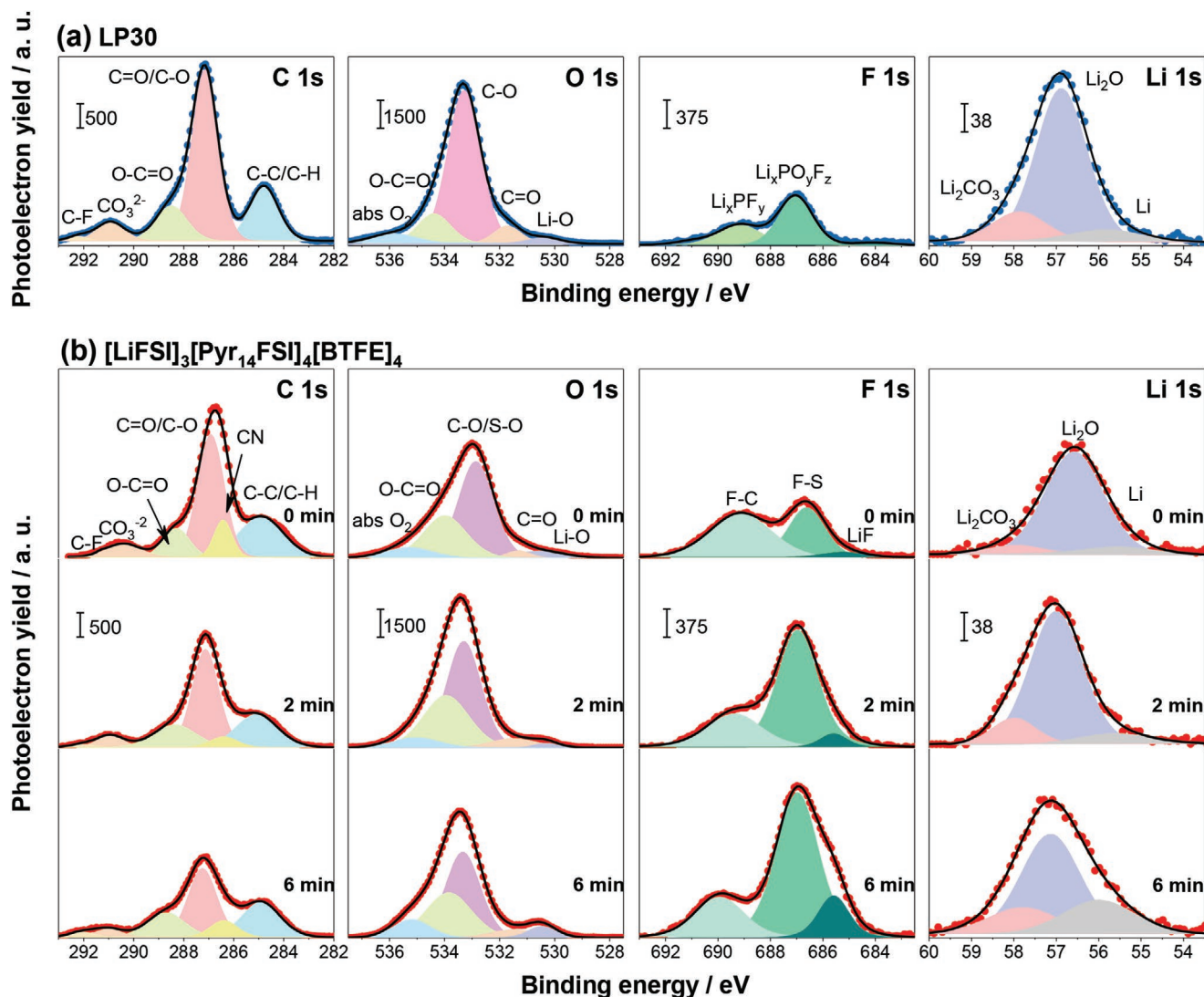
ADVANCED
SCIENCE NEWS
www.advancedsciencenews.com

small
methods
www.small-methods.com

Figure 5. XPS analysis of C 1s, O 1s, F 1s, and Li 1s photoelectron lines for the Li (1.5 mAh cm^{-2}) deposited on Cu foil at 0.5 mA cm^{-2} in a) the LP30 electrolyte (without Ar$^+$ sputtering) and in b) the Li$_3$Py$_4$BT$_4$ electrolyte (surface and after Ar$^+$ sputtering for 2 and 6 min).

2.6. High Efficient LMBs

Li/LFP coin cells were assembled to verify the compatibility of the developed electrolyte in LMBs. LFP was initially selected as the cathode material because of its superior cycling stability and rate capability. Moreover, the low potential cut-off used in LFP cells limits the oxidative degradation phenomena. In such a condition, we can mostly associate the cell degradation phenomena to LMA instability.[56] The used LFP electrodes had a relevant active material areal loading of 6.3 mg cm^{-2}, corresponding to an areal capacity of 1 mAh cm^{-2}. The CV curves of the Li/LFP cell employing Li$_3$Py$_4$BT$_4$ at 20 °C are shown in Figure S9, Supporting Information.

Figure 6a reports the cell's rate capability and discharge specific capacities behavior. At 0.1 C (1 C = 160 mA g^{-1} ≈ 1 mA cm^{-2}), the cells using LP30 and Li$_3$Py$_4$BT$_4$ show a slightly higher specific capacity than those employing Li$_1$Py$_4$ and Li$_3$Py$_4$ electrolytes. After a few cycles, the cells employing Li$_1$Py$_4$ and

Li$_3$Py$_4$ cannot reach the 4.0 V upper cut-off (Figure S10, Supporting Information), indicating an internal short-circuit upon lithium plating. On the contrary, the cell employing Li$_3$Py$_4$BT$_4$ operates well even at 2 C (≈2 mA cm^{-2}), delivering a specific capacity of about 130 mAh g^{-1}, which reveals an excellent rate capability. However, the cell employing LP30 shows a better response at high current (>1 C) with respect to the Li$_3$Py$_4$BT$_4$ one, most likely due to the relatively higher viscosity and lower conductivity of the later. The dis-/charge profiles of these two cells at selected current rates are displayed in Figure 6b. Due to the inferior ionic conductivity of Li$_3$Py$_4$BT$_4$ versus LP30 (Tables S1,S2,S4, Supporting Information), the cell employing Li$_3$Py$_4$BT$_4$ exhibits relatively worse high rate capability.

Figure 6c displays the *CE* and average polarization at different current rates. Although the ionic conductivity of Li$_3$Py$_4$BT$_4$ is inferior to that of LP30, the average polarization gap between cells employing the two electrolytes is not wide. Even at 2 C, the gap is only 41 mV, which matches well with the polarization
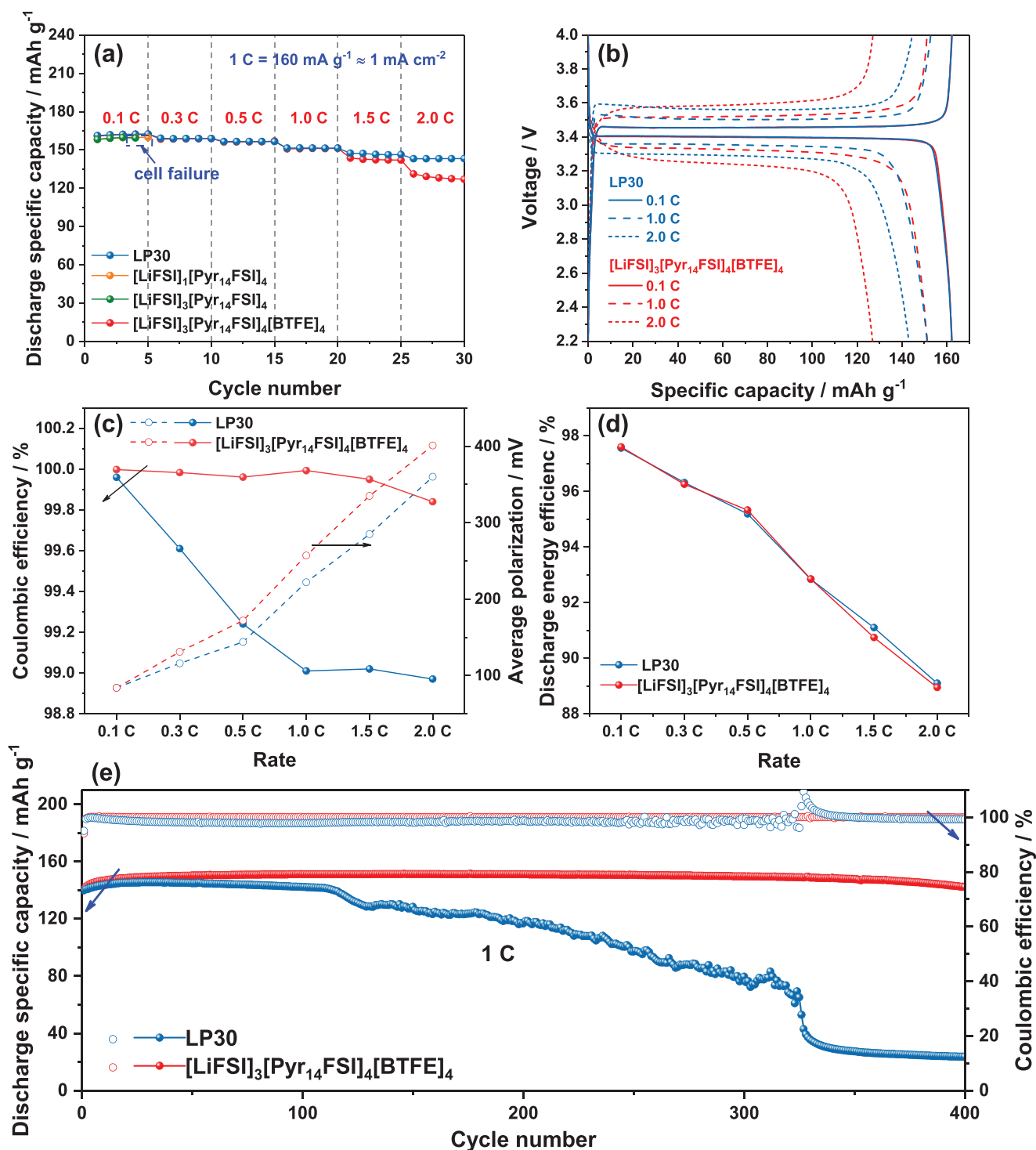
ADVANCED
SCIENCE NEWS
www.advancedsciencenews.com

small
methods
www.small-methods.com

Figure 6. a) Rate performance of the Li/LFP cells employing the LP30 and IL-based electrolytes. b) The discharge/charge profiles of the Li/LFP cell using the $Li_3Py_4BT_4$ and LP30 electrolyte at 0.1, 1.0, and 2.0 C. c) The CE and average polarization of the Li/LFP cells employing the LP30 and $Li_3Py_4BT_4$ electrolytes at different current rates. d) The discharge energy efficiency of the Li/LFP cells employing the LP30 and $Li_3Py_4BT_4$ electrolytes. e) The evolution of CE and discharge specific capacity upon long-term cycling of Li/LFP cells employing the LP30 and $Li_3Py_4BT_4$ electrolytes at 1 C. The mass loading of LFP is 6.3 mg cm^{-2}. 1 C = 160 mA g$^{-1} \approx$ 1 mA cm^{-2}.

of Li/Li symmetric cells (see Figure 3c). On the other hand, $Li_3Py_4BT_4$ leads to higher CE. When the specific current is lower than 1.5 C, the CE is higher than 99.95%, and a slightly lower CE, that is, 99.8%, is still attained at 2 C. With LP30, the CE at 1 C is 99%. Figure 6d compares the energy efficiency, revealing similar values for both systems, for example, 92.8% at 1 C.

The long-term cyclability of Li/LFP cells employing $Li_3Py_4BT_4$ and LP30 was evaluated at 1 C rate. The evolution of the discharge specific capacity and *CE* is shown in Figure 6e. As expected, the cell employing LP30 exhibits a cycle life (80% retention of the initial capacity) of only 218 cycles with an average *CE* of 98.27%. When the $Li_3Py_4BT_4$ is employed as the electrolyte, the Li/LFP cell's cycle life is thoroughly improved. The specific capacity of LFP increases from the initial 141 to 150 mAh g^{-1} at around the 100th cycle and reaches 142 mAh g^{-1} at the 400th cycle, showing a remarkable capacity retention of 94.6%. Upon cycling, the average *CE* is 99.97%, demonstrating high reversibility. The dis-/charge profiles and discharge energy efficiencies at selected cycles are shown in Figure S11, Supporting Information. The energy efficiency of the cell employing LP30 rapidly drops from 93.6% at the 20th cycle to 83.8% at the 220th cycle, due to the degradation of LMA. On the contrary, the cell employing $Li_3Py_4BT_4$ shows a gradual energy efficiency decrease from 92.7% at the 20th cycle to 88.8% at the 400th cycle, with an average value in the 400 cycles of 90.88%. The improved performance clearly results from a more stable LMAs in the $Li_3Py_4BT_4$ electrolyte.

Li/$Li_3Py_4BT_4$/LFP cells' rate performance was also evaluated at various temperatures to assess the cell temperature operative range. The results are summarized in **Figure 7**a. At increased temperature, that is, 40 °C, a better rate capability is displayed due to the reduced viscosity and enhanced ionic conductivity (as shown in Figure 1d,e, respectively). At 3 C, ≈3 mA cm^{-2}, the LFP cathode reaches 140 mAh g^{-1}. As expected, the temperature

decrease leads to reduced delivered capacities resulting from a lower ionic conductivity of the electrolyte. For example, at 0.5 C, the specific capacity is 156, 139, 126, and 91 mAh g^{-1} at 40, 10, 0, and −10 °C, respectively. The dis-/charge profiles at different current rates are displayed in Figure 7b and Figure S12, Supporting Information. These results demonstrate a wide operating temperature of the Li/ $Li_3Py_4BT_4$/LFP cells.

Nickel-rich cathodes ($LiNi_xMn_yCo_{1-x-y}O_2$, NMC, $x \geq 0.5$) are the targeted positive electrodes for high energy density LMBs, due to the high capacity, elevated operative voltage, and high tap density. Li/NMC532 cells were assembled to assess the compatibility of the developed electrolyte with this high-voltage cathode material. The mass loading of the NMC532 was 7.6 mg cm^{-2}. The CV curves of the Li/NMC532 cell employing $Li_3Py_4BT_4$ at 20 °C are shown in Figure S13, Supporting Information. After two activation cycles at 0.1 C (1 C = 160 mA $g^{-1} \approx 1.2$ mA cm^{-2}), the cell was cycled with a charge rate of 1/3 C and a discharge rate of 1 C. The results are shown in Figure 7c. The discharge capacity at the 150th cycle is 93.9% of the one at the 3rd cycle, and the average *CE* upon cycling is 99.91% (from 4th to 150th), indicating for a good compatibility of $Li_3Py_4BT_4$ with the nickel-rich cathode. The dis-/charge profiles at the selected cycles are shown in Figure 7d. The relatively lower average *CE* in Li/NMC cells versus Li/LFP cells demonstrates accelerated side reactions on the cathode/electrolyte interface because of a higher operation potential and NMC's catalytic effect in enhancing the electrolyte decomposition.[57] Considering the anodic stability potential window of the electrolyte and the current per-
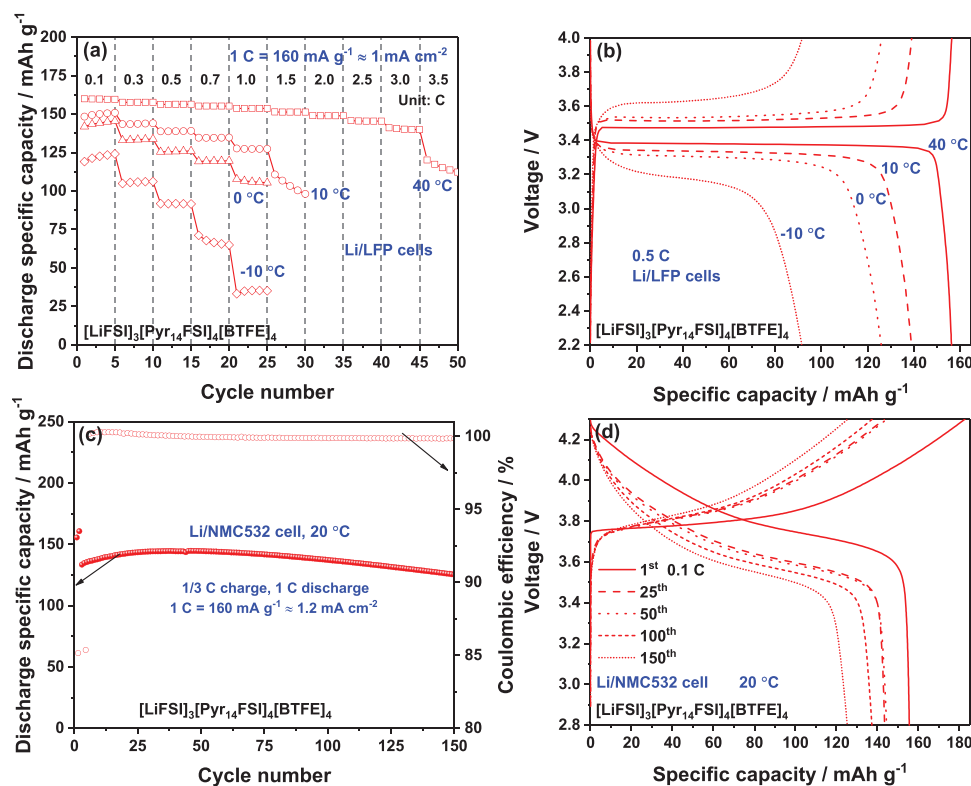

Figure 7. Rate performance of the Li/LFP cells employing $Li_3Py_4BT_4$ at different operation temperature: a) The discharge specific capacity of the LFP cathode upon the measurements and b) the dis-/charge profiles at 0.5 C. Cyclability of the Li/NMC532 cell employing $Li_3Py_4BT_4$ at 20 °C: c) The evolution of *CE* and discharge specific capacity upon cycling and d) the discharge/charge profiles at the selected cycles.

ADVANCED
SCIENCE NEWS
www.advancedsciencenews.com

small
methods
www.small-methods.com

formance, we can infer that further optimization of the cathode material, for example, the structure, morphology, and surface engineering,[58] as well as the electrolyte, for example, different fluorinated ether,[29,44] and use of additives, is feasible to improve the performance of the Li/NMC cells.

3. Conclusion

The addition of BTFE to the IL-based electrolytes, employing the FSI^- anion, can effectively improve Li^+ transports. Meanwhile, high compatibility with LMAs is not affected. The promoted Li^+ transport in the optimized electrolyte, $[LiFSI]_3[Pyr_{14}FSI]_4[BTFE]_4$, originates from the high-level Li^+-FSI^- ion-pairing and low solution viscosity, which are associated with the high molar ratio of $LiFSI:Pyr_{14}FSI$, and the non-solvating character and low viscosity of BTFE. The decomposition products of BTFE constitute the matrix of the SEI on Li. The FSI^- and Pyr_{14}^+ decomposition products are mainly present in the SEI's inner and outer layers, respectively. The use of $Li_3Py_4BT_4$ as the electrolyte in Li/LFP cells guarantees improved cycle life with respect to commercial LP30, and a wide operating temperature. Additionally, the $Li_3Py_4BT_4$ electrolyte shows good compatibility with 4 V-class NMC cathodes. The insight into the enhanced Li^+ transports and SEI characteristics gives fundamental information essential for further developing IL-based electrolytes for safe and more practical LMBs.

4. Experimental Section

Materials: Molecular sieves (3 Å, Alfa Aesar) were activated at 300 °C under vacuum (10^{-3} mbar) for more than one week. BTFE (98%, Sigma Aldrich) and DMC (Battery grade, UBE) were dried with the activated molecular sieves for three days before use. LiFSI (99%, PROVISCO CS) was dried at 120 °C under vacuum (10^{-3} mbar) for 24 h before use. $Pyr_{14}FSI$ prepared via previously reported methods was dried stepwise from room temperature to 60 °C in vacuum range of 10^{-7} mbar for 3 days.[15] Carbon coated LFP (M23, Advanced Lithium Electrochemistry Co., Ltd.), NMC532 (BASF), lithium metal foil (thickness 500 μm, Honji Metal Co., LTD), carbon black (Super C65, IMERYS Graphite & Carbon), *N*-methyl-2-pyrrolidone (NMP, anhydrous, Sigma Aldrich), and polyvinylidene fluoride (PVdF, Solef6020), LP30 (Battery grade, BASF) were used as received. Glass fiber sheet (Whatman GF/A) and PE sheet (SV718, Asahi Kasei Company) were dried at 150 and 40 °C, respectively, under vacuum (10^{-3} mbar) for 24 h.

Electrolyte and Electrode Preparation: The electrolyte preparation was carried out in an Ar-filled glove box with H_2O and O_2 levels <0.1 ppm. For $LiFSI-Pyr_{14}FSI$ binary electrolytes, the dried LiFSI was dissolved in the dried $Pyr_{14}FSI$, and further dried at 60 °C in vacuum range of 10^{-7} mbar for 3 days. The $LiFSI-Pyr_{14}FSI-BTFE/DMC$ ternary electrolytes were prepared via mixing the fully dried $LiFSI-Pyr_{14}FSI$ binary electrolytes with corresponding, pre-dried solvents, that is, BTFE, or DMC. LFP and NMC532 electrodes were fabricated via doctor-blade casting of the NMP-based slurries containing 90 wt% active material (LFP or NMC532), 5 wt% C65, and 5 wt% PVdF binder on carbon-coated Al foil. After the evaporation of NMP solvent in an oven at 80 °C, the electrodes with a diameter of 12 mm were punched and further dried at 110 °C under vacuum (10^{-3} mbar) for 12 h. After being weighed in a dry room where the dew point was below −70 °C (H_2O level < 1 ppm), the electrodes were dried at 110 °C under vacuum (10^{-3} mbar) for another 4 h, and then transferred to the Ar-filled glovebox. The average mass loading of LFP and NMC was 6.3 and 7.6 mg cm^{-2}, respectively. For the fabrication of

C65 electrodes, similar procedures were used, but the composition of C65 and PVdF was 80 and 20 wt%, respectively, and Al foil was used as the current collector.

Characterizations: The conductivity of the electrolytes were determined via electrochemical impedance spectroscopy by an integrated liquid conductivity system MCS 10 (Material Mates-Biologic) sealed high temperature conductivity cells (HTCC, Material Mates) with Pt-black electrodes were used. The conductivity values averaged over 60 min (around 60 data points) were used. The cell constants were determined using a 0.01 M KCl standard solution. The electrolytes' viscosity was tested in a dry room environment utilizing an Anton-Paar MCR 102 rheometer, applying a constant shear rate of 10 s^{-1}, and using a Peltier system for cooling/heating. The viscosity values averaged over 2.5 min (50 data points) were used. The Raman measurements were recorded on a RAM II FT-Raman module of a Bruker Vertex70v FT-IR spectrometer with a laser wavelength of 1064 nm and laser power of 300 mW. SAXS patterns were collected at the SWING beamline 1 of the Soleil Synchrotron near Paris (France), with monochromator set at 16 KeV. Using a EIGERX 4M detector at 0.871 m from the sample, diffraction patterns were recorded for reciprocal spacing $q = 4\pi \sin(\theta)/\lambda$ varying between 0.0126 and 1.4 $Å^{-1}$, that is, repetitive distances $d = 2\pi/q$ ranging from 500 to 5 Å. Beam size was 375×25 μm² ($V \times H$).To ensure the best background subtraction, the empty 1.5 mm o.d. (1.48 mm i.d.) quartz capillaries were measured before the sample injection, and each background was used on the corresponding sample, even if the difference between the scattering patterns of the empty capillary was negligible. The samples were injected into capillaries, which were sealed with epoxy glue to avoid evaporation and water contamination. The exposure time was set to 500 ms and five consequent patterns were collected and 1D SAXS curves were obtained by circular averaging of the 2D images using the Foxtrot software. SEM images were obtained using a Zeiss LEO 1550 microscope. The cross section of the lithium electrodes was made with a scissor in the glove box. XPS measurements were conducted in an ultrahigh vacuum surface analysis system (10^{-10} mbar) by Phoibos 150 XPS spectrometer (SPECS-Surface concept) equipped with a micro-channel plate and Delay Line Detector and monochromatized Al Kα (1486.6 eV) X-ray in a fixed analyzer transmission mode. The scans were acquired with an X-ray sources of 200 W, 30 eV pass energy and 0.1 eV energy step. The depth profiling was carried out using a focused ion gun for 5 keV Ar^+, for 2 and 6 min. The photoelectron spectra were calibrated using C−C/C−H peak at 284.8 eV as reference. The peak fitting was carried out by CasaXPS software, using Shiley-type background and 70% Gaussian–30% Lorentzian profile function. For the post-mortem characterization, the electrodes were removed from cells and washed with dried DMC in the Ar-filled glove box. The samples were sealed in transfer boxes to prevent exposure to humid air for SEM and XPS measurements.

Electrochemical Measurements: For Swagelok T cells, GF/A discs (diameter: 13 mm) and lithium discs (diameter: 12 mm) were used as the separators and the counter electrodes, respectively, and 120 μL electrolytes were added for each cell. For CR2032-type coin cells, lithium discs with a diameter of 14 mm were used as the negative electrode, and 50 μL electrolytes were added to each cell. For the coin cells employing LP30 or $LiFSI-Pyr_{14}FSI-BTFE/TTE/DMC$ ternary electrolytes, the PE discs were used as the separator, while the GF/A discs were used as the separator for the ones employing $LiFSI-Pyr_{14}FSI$ binary electrolytes. The electrolytes' electrochemical anodic stability was evaluated by linear sweep voltammetry (scan rate of 0.1 mV s^{-1}) using Swagelok T-cells employing the C65-coated Al foil as the working electrode at 20 °C with a galvanostat/potentiostat VMP (Bio-Logic). The Li CE in the different electrolytes was measured in Li/Cu coin cells, in which a copper foil with a diameter of 19 mm was used as the working electrode.[59] For Li/LFP, and Li/NMC cells, the Cu foil was replaced with LFP or NMC electrodes, respectively. Without further notification, the measurements were conducted at 20 °C with a Maccor series 4000 battery cycler. To evaluate the impedance evolution of the Li/Li coin cells employing different electrolytes upon cycling, the measurements were conducted with the VMP. The Li/LFP cells' rate performance at 40 °C was measured via the Maccor battery cycler, while those at −10, 0, and 10 °C were measured

with the VMP. The temperature of the cells during the measurements were controlled and maintained via Binder ovens.

Supporting Information

Supporting Information is available from the Wiley Online Library or from the author.

Acknowledgements

Conflict of Interest

The authors declare no conflict of interest.

Data Availability Statement

Research data are not shared.

Keywords

[1] J. Xiao, Q. Li, Y. Bi, M. Cai, B. Dunn, T. Glossmann, J. Liu, T. Osaka, R. Sugiura, B. Wu, J. Yang, J. G. Zhang, M. S. Whittingham, *Nat. Energy* **2020**, *5*, 561.

[2] W. Xu, J. Wang, F. Ding, X. Chen, E. Nasybulin, Y. Zhang, J. G. Zhang, *Energy Environ. Sci.* **2014**, *7*, 513.

[3] G. Xu, L. Huang, C. Lu, X. Zhou, G. Cui, *Energy Storage Mater.* **2020**, *31*, 72.

[4] D. Lin, Y. Liu, Z. Liang, H. W. Lee, J. Sun, H. Wang, K. Yan, J. Xie, Y. Cui, *Nat. Nanotechnol.* **2016**, *11*, 626.

[5] X. Liang, Q. Pang, I. R. Kochetkov, M. S. Sempere, H. Huang, X. Sun, L. F. Nazar, *Nat. Energy* **2017**, *2*, 17119.

[6] Z. Wang, F. Qi, L. Yin, Y. Shi, C. Sun, B. An, H. M. Cheng, F. Li, *Adv. Energy Mater.* **2020**, *10*, 1903843.

[7] J. Liu, Z. Bao, Y. Cui, E. J. Dufek, J. B. Goodenough, P. Khalifah, Q. Li, B. Y. Liaw, P. Liu, A. Manthiram, Y. S. Meng, V. R. Subramanian, M. F. Toney, V. V. Viswanathan, M. S. Whittingham, J. Xiao, W. Xu, J. Yang, X. Q. Yang, J. G. Zhang, *Nat. Energy* **2019**, *4*, 180.

[8] D. R. MacFarlane, M. Forsyth, P. C. Howlett, M. Kar, S. Passerini, J. M. Pringle, H. Ohno, M. Watanabe, F. Yan, W. Zheng, S. Zhang, J. Zhang, *Nat. Rev. Mater.* **2016**, *1*, 15005.

[9] J. Huang, A. F. Hollenkamp, *J. Phys. Chem. C* **2010**, *114*, 21840.

[10] J. N. C. Lopes, K. Shimizu, A. A. H. Pádua, Y. Umebayashi, S. Fukuda, K. Fujii, S. I. Ishiguro, *J. Phys. Chem. B* **2008**, *112*, 9449.

[11] G. A. Elia, U. Ulissi, S. Jeong, S. Passerini, J. Hassoun, *Energy Environ. Sci.* **2016**, *9*, 3210.

[12] N. Xiao, G. Gourdin, Y. Wu, *Angew. Chem., Int. Ed.* **2018**, *57*, 10864.

[13] W. Xue, Z. Shi, M. Huang, S. Feng, C. Wang, F. Wang, J. Lopez, B. Qiao, G. Xu, W. Zhang, Y. Dong, R. Gao, Y. Shao-Horn, J. A. Johnson, J. Li, *Energy Environ. Sci.* **2020**, *13*, 212.

[14] L. Grande, J. Von Zamory, S. L. Koch, J. Kalhoff, E. Paillard, S. Passerini, *ACS Appl. Mater. Interfaces* **2015**, *7*, 5950.

[15] E. Paillard, Q. Zhou, W. A. Henderson, G. B. Appetecchi, M. Montanino, S. Passerini, *J. Electrochem. Soc.* **2009**, *156*, A891.

[16] M. Kirchhöfer, J. Von Zamory, E. Paillard, S. Passerini, *Int. J. Mol. Sci.* **2014**, *15*, 14868.

[17] U. Pal, F. Chen, D. Gyabang, T. Pathirana, B. Roy, R. Kerr, D. R. MacFarlane, M. Armand, P. C. Howlett, M. Forsyth, *J. Mater. Chem. A* **2020**, *8*, 18826.

[18] K. Dokko, N. Tachikawa, K. Yamauchi, M. Tsuchiya, A. Yamazaki, E. Takashima, J.-W. Park, K. Ueno, S. Seki, N. Serizawa, M. Watanabe, *J. Electrochem. Soc.* **2013**, *160*, A1304.

[19] M. L. Gordin, F. Dai, S. Chen, T. Xu, J. Song, D. Tang, N. Azimi, Z. Zhang, D. Wang, *ACS Appl. Mater. Interfaces* **2014**, *6*, 8006.

[20] S. Chen, J. Zheng, D. Mei, K. S. Han, M. H. Engelhard, W. Zhao, W. Xu, J. Liu, J. G. Zhang, *Adv. Mater.* **2018**, *30*, 1706102.

[21] X. Ren, S. Chen, H. Lee, D. Mei, M. H. Engelhard, S. D. Burton, W. Zhao, J. Zheng, Q. Li, M. S. Ding, M. Schroeder, J. Alvarado, K. Xu, Y. S. Meng, J. Liu, J. G. Zhang, W. Xu, *Chem* **2018**, *4*, 1877.

[22] S. Chen, J. Zheng, L. Yu, X. Ren, M. H. Engelhard, C. Niu, H. Lee, W. Xu, J. Xiao, J. Liu, J. G. Zhang, *Joule* **2018**, *2*, 1548.

[23] N. Piao, X. Ji, H. Xu, X. Fan, L. Chen, S. Liu, M. N. Garaga, S. G. Greenbaum, L. Wang, C. Wang, X. He, *Adv. Energy Mater.* **2020**, *10*, 1903568.

[24] X. Cao, X. Ren, L. Zou, M. H. Engelhard, W. Huang, H. Wang, B. E. Matthews, H. Lee, C. Niu, B. W. Arey, Y. Cui, C. Wang, J. Xiao, J. Liu, W. Xu, J. G. Zhang, *Nat. Energy* **2019**, *4*, 796.

[25] T. Doi, Y. Shimizu, M. Hashinokuchi, M. Inaba, *J. Electrochem. Soc.* **2017**, *164*, A6412.

[26] L. Lombardo, S. Brutti, M. A. Navarra, S. Panero, P. Reale, *J. Power Sources* **2013**, *227*, 8.

[27] S. Zugmann, M. Fleischmann, M. Amereller, R. M. Gschwind, H. D. Wiemhöfer, H. J. Gores, *Electrochim. Acta* **2011**, *56*, 3926.

[28] H. Yoon, P. C. Howlett, A. S. Best, M. Forsyth, D. R. MacFarlane, *J. Electrochem. Soc.* **2013**, *160*, A1629.

[29] C. C. Su, M. He, R. Amine, K. Amine, *Angew. Chem., Int. Ed.* **2019**, *58*, 10591.

[30] C. Schreiner, S. Zugmann, R. Hartl, H. J. Gores, *J. Chem. Eng. Data* **2010**, *55*, 1784.

[31] L. R. Bard, J. Allen, Faulkner, *Electrochemical Methods: Fundamentals and Applications*, Wiley, New York **2001**.

[32] X. Gao, F. Wu, A. Mariani, S. Passerini, *ChemSusChem* **2019**, *12*, 4185.

[33] M. Beran, J. Příhoda, Z. Žák, M. Černík, *Polyhedron* **2006**, *25*, 1292.

[34] Y. Yamada, A. Yamada, *J. Electrochem. Soc.* **2015**, *162*, A2406.

[35] H. Yoon, A. S. Best, M. Forsyth, D. R. MacFarlane, P. C. Howlett, *Phys. Chem. Chem. Phys.* **2015**, *17*, 4656.

[36] X. Gao, A. Mariani, S. Jeong, X. Liu, X. Dou, M. Ding, A. Moretti, S. Passerini, *J. Power Sources* **2019**, *423*, 52.

[37] K. Fujii, S. Seki, S. Fukuda, T. Takamuku, S. Kohara, Y. Kameda, Y. Umebayashi, S. ichi Ishiguro, *J. Mol. Liq.* **2008**, *143*, 64.

[38] K. Fujil, S. Seki, S. Fukuda, R. Kanzaki, T. Takamuku, Y. Umebayashi, S. I. Ishiguro, *J. Phys. Chem. B* **2007**, *111*, 12829.

[39] J. Zheng, S. Chen, W. Zhao, J. Song, M. H. Engelhard, J. G. Zhang, *ACS Energy Lett.* **2018**, *3*, 315.

[40] A. Mariani, P. Ballirano, F. Angiolari, R. Caminiti, L. Gontrani, *ChemPhysChem* **2016**, *17*, 3023.

[41] P. Calandra, *J. Mol. Liq.* **2020**, *310*, 113186.

[42] J. N. A. Canongia Lopes, A. A. H. Pádua, *J. Phys. Chem. B* **2006**, *110*, 3330.

[43] A. Mariani, R. Caminiti, M. Campetella, L. Gontrani, *Phys. Chem. Chem. Phys.* **2016**, *18*, 2297.

[44] A. Bouibes, S. Saha, M. Nagaoka, *Sci. Rep.* **2020**, *10*, 21966.

[45] Y. Yamada, J. Wang, S. Ko, E. Watanabe, A. Yamada, *Nat. Energy* **2019**, *4*, 269.

[46] M. Eftekharnia, M. Hasanpoor, M. Forsyth, R. Kerr, P. C. Howlett, *ACS Appl. Energy Mater.* **2019**, *2*, 6655.

[47] G. Bieker, M. Winter, P. Bieker, *Phys. Chem. Chem. Phys.* **2015**, *17*, 8670.

[48] J.-J. Woo, V. A. Maroni, G. Liu, J. T. Vaughey, D. J. Gosztola, K. Amine, Z. Zhang, *J. Electrochem. Soc.* **2014**, *161*, A827.

[49] A. M. Andersson, A. Henningson, H. Siegbahn, U. Jansson, K. Edström, *J. Power Sources* **2003**, *119*, 522.

[50] S. Malmgren, K. Ciosek, M. Hahlin, T. Gustafsson, M. Gorgoi, H. Rensmo, K. Edström, *Electrochim. Acta* **2013**, *97*, 23.

[51] K. Edström, T. Gustafsson, J. O. Thomas, *Electrochim. Acta* **2004**, *50*, 397.

[52] J. Chen, Q. Li, T. P. Pollard, X. Fan, O. Borodin, C. Wang, *Mater. Today* **2020**, *39*, 118.

[53] H. Ota, Y. Sakata, X. Wang, J. Sasahara, E. Yasukawa, *J. Electrochem. Soc.* **2004**, *151*, A437.

[54] X. Fan, L. Chen, X. Ji, T. Deng, S. Hou, J. Chen, J. Zheng, F. Wang, J. Jiang, K. Xu, C. Wang, *Chem* **2018**, *4*, 174.

[55] T. Li, X. Q. Zhang, P. Shi, Q. Zhang, *Joule* **2019**, *3*, 2647.

[56] Q. Zhang, S. Liu, Z. Lin, K. Wang, M. Chen, K. Xu, W. Li, *Nano Energy* **2020**, *74*, 104860.

[57] H. H. Sun, H. H. Ryu, U. H. Kim, J. A. Weeks, A. Heller, Y. K. Sun, C. B. Mullins, *ACS Energy Lett.* **2020**, *5*, 1136.

[58] J. U. Choi, N. Voronina, Y. K. Sun, S. T. Myung, *Adv. Energy Mater.* **2020**, *10*, 2002027.

[59] B. D. Adams, J. Zheng, X. Ren, W. Xu, J. G. Zhang, *Adv. Energy Mater.* **2018**, *8*, 1702097.